

Multimode Detection of Hydrogen Gas Using Palladium-Covered Silicon μ -Channels

G. Kaltenpoth,[†] P. Schnabel,[‡] E. Menke,[§] E. C. Walter,[§] M. Grunze,[†] and R. M. Penner^{*,§}

Department of Chemistry, University of California, Irvine, California 92697-2025, Angewandte Physikalische Chemie, Universität Heidelberg, Im Neuenheimer Feld 253, D-69120 Heidelberg, Germany, and Charles Evans & Associates, 810 Kifer Road, Sunnyvale, California 94086

Palladium was electrodeposited onto lithographically patterned Si(100) “ μ -channels” with dimensions of 2 μm (width) \times 100 μm (length). The properties of these Pd-covered Si μ -channels for detecting dihydrogen gas were then evaluated. Pd electrodeposition was carried out under conditions favoring an instantaneous nucleation and growth mechanism. This strategy produced size-similar Pd particles at a coverage of $(4\text{--}6) \times 10^9 \text{ cm}^{-2}$ within the confines of the Si μ -channel. When the mean particle radius, r_0 , was smaller than a critical value ($r_0 < r_c = 70\text{--}85 \text{ nm}$), each Pd particle was well separated on the surface from adjacent particles, on average, and no response to H_2 gas attributable to the μ -channel was observed. As Pd particles were grown larger, to a mean radius of $r_0 \approx r_c$, adjacent particles on the surface touched and the electrical resistance of the μ -channel dropped by several orders of magnitude. These “type 2” H_2 sensors exhibited a rapid ($<1 \text{ s}$), reversible decrease in their resistance in response to exposure to H_2 above 0.5%, but a minimum resistance was observed at 1–2%, and a resistance increase was seen at higher H_2 concentration. This complex behavior resulted from the existence of three mechanisms for charge transport across the μ -channel. If still larger quantities of Pd were deposited, the Pd particle ensemble coalesced into an electrically continuous film. These “type 3” sensors became more resistive in the presence of H_2 , not more conductive as seen for sensors of types 1 and 2, but the amplitude of this response was smaller than seen for type 2 sensors.

When automobiles powered by hydrogen gas eventually become available, they will be equipped with sensors designed solely to warn the occupants of the car in the eventuality of a H_2 gas leak. Ideally, these H_2 “safety sensors” will be capable of detecting leaked H_2 gas at concentrations of 1.0% or less, well below the lower explosion limit of H_2 in air of 4%. They will also be fast ($t < 1 \text{ s}$), dependable over a wide temperature range (0–100 $^\circ\text{C}$), power efficient ($<1 \text{ W}$), and low cost since each car will have multiple sensors of this type. Surprisingly, these requirements test the capabilities of state-of-the-art H_2 sensors.

For example, the Robust Wide-Range H_2 Sensor technology, developed in the early 1990s by Hughes at Sandia National Laboratories, uses a field effect transistor with a palladium–nickel alloy gate^{1,2} in parallel with a PdNi resistor. Commercial versions of this sensor³ are capable of accurately measuring H_2 from 0.0001–100%, but they are both expensive (\$500 per sensing point) and too slow to respond at low H_2 concentrations ($<1\%$).

In principle, the complexity and cost of existing sensors could be reduced if multiple sensing mechanisms could be incorporated into a single device. This paper represents our first exploration of this concept. “Multimode” H_2 sensors were realized by electrodepositing conductive networks of Pd nanoparticles onto 2.0- μm -wide, 0.12- μm -deep, and 100- μm -long Si(100) channels (or “ μ -channels”) prepared by optical lithography. By measuring the resistance of these Pd-covered Si μ -channels in air and in H_2 as a function of the palladium coverage, we have attempted to understand the origin of the observed sensor responses. We conclude that the conductivity change seen for these Pd-covered μ -channels upon exposure to H_2 is caused by the confluence of as many as three mechanisms. Three distinctly different types of H_2 sensors were observed depending on the Pd coverage within the μ -channel, but none of these had properties that would be suitable for general-purpose H_2 sensing. However, one of these (obtained for intermediate Pd coverages) had a response to H_2 at low concentrations (LOD $\approx 0.5\% \text{ H}_2$) that was fast (1-s turn-on) and reversible—attributes required for H_2 safety sensing applications.

EXPERIMENTAL SECTION

Lithography. The optical lithography scheme employed here is summarized in Scheme 1. Silicon wafers were 4-in.-diameter n-type Si(100) wafers (FZ, phosphorus doped, resistivity 75–125 $\Omega \text{ cm}$, thickness $300 \pm 10 \mu\text{m}$, Wacker Siltronic AG). Onto each wafer was deposited a $\sim 0.125\text{-}\mu\text{m}$ SiO_2 layer using plasma-enhanced chemical vapor deposition (PECVD). This was accomplished using a Plasmatherm 790 Series with the precursor gases N_2O , SiH_4 , and N_2 at an rf frequency of 13.56 MHz, a power of 20 W, and a substrate temperature of 240 $^\circ\text{C}$. Next, a S1808 photoresist (Shipley) was spin-coated onto the primed (10% hexamethyldisilazane in acetone as adhesion promoter) wafers,

* Corresponding author. E-mail: rmpenner@uci.edu.

[†] Universität Heidelberg.

[‡] Charles Evans & Associates.

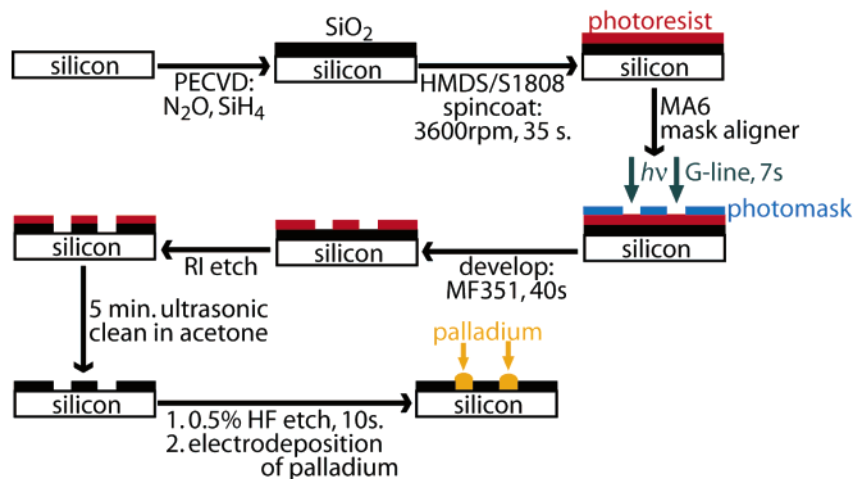
[§] University of California.

(1) Hughes, R. C. *J. Electrochem. Soc.* **1984**, *131*, C322.

(2) Ruths, P. F.; Ashok, S.; Fonash, S. J.; Ruths, J. M. *IEEE Trans. Electron Devices* **1981**, *ED28*, 1003.

(3) Manufactured most recently by DCH Inc., Valencia, CA.

Scheme 1



leading to an approximate resist thickness of 0.9–1.0 μm . After the soft baking (20 min at 90 $^{\circ}\text{C}$), samples were exposed to G-line UV for 7 s in a MA6 mask aligner (Karl Suss). The exposed wafers were then developed for 40 s with MF319 developer (Shipley), rinsed with Millipore water, and baked 20 min at 120 $^{\circ}\text{C}$. Reactive ion (RI) etching was then used to remove the exposed PECVD SiO_2 layer. The RI etching was carried out in a Plasmatherm 790 Series with the precursor gases CF_4 and O_2 at an rf power of 170 W at room temperature. Finally, the photoresist remaining on nonexposed areas of the wafer was removed by ultrasonically cleaning each wafer in acetone for 5 min. The resulting “device pattern”, shown in Figure 1, consisted of Si(100) “channels” (width 2 μm ; depth 0.12 μm , length 100 μm) connected to 1.4 \times 1.4 mm

Si(100) pads (area 2 mm²) surrounded by PECVD SiO_2 (see Scheme 1).

Preparation of Patterned Si for Electrodeposition. The patterned Si wafers were cut into $\sim 1 \times 1$ cm squares containing four device patterns. An ohmic contact was applied to the back of this square using GaIn eutectic. Conductive silver paint (Ted Pella, Inc.) was then used to attach a conductive copper tape (Ted Pella) to this contact. Finally, a chemically resistant epoxy (Loctite 1C Hysol) was applied to the back and edges of the Si square so that just the patterned surface was exposed to the Pd plating solution.

Electrochemistry. All chemicals were reagent grade from Fisher and were used without further purification. The Pd plating solution consisted of 1 mM $\text{Pd}(\text{NO}_3)_2$, 0.5 M HClO_4 , and 10 mM NH_4F in Nanopure deionized water ($\rho > 17.8$ M Ω cm). The Pd plating solution was purged for 10 min with prehumidified N_2 prior to use. Cyclic voltammograms and potentiostatic metal plating pulses were acquired using a Princeton Applied Research ParStat 2263 potentiostat. All deposition experiments were carried out in a glass electrochemical cell. Immediately prior to each deposition experiment, the Si square working electrode was exposed to a dilute 0.5% HF (aq) etch that removed any native oxide from the device pattern without compromising the PECVD SiO_2 . A saturated calomel reference electrode (SCE) and a platinum foil (~ 1 cm²) counter electrode were used in all experiments. After each deposition, Si electrodes were rinsed with Nanopure water, dried with nitrogen, and stored under dry argon.

Microscopy. Samples to be examined using the scanning electron microscopy (SEM) were mounted onto aluminum SEM stubs using adhesive carbon dots (Ted Pella, Inc.). An electrical contact between sample and SEM stub was established using silver paint and conductive copper tape. Scanning electron microscopy and energy-dispersive X-ray analyses were carried out using a Philips model XL-30FEG operating at 10 keV.

Scanning Auger Microprobe. Scanning Auger micrographs were acquired on a Physical Electronics Smart 200 Field Emission Nanoprobe. The primary electron beam energy was 20 keV, and the incident angle was 30 $^{\circ}$ with respect to the surface normal. For Si and C, the KLL transitions used were at 1620 and 275 eV, respectively. To monitor Pd, the MNN transition at 333 eV was selected.

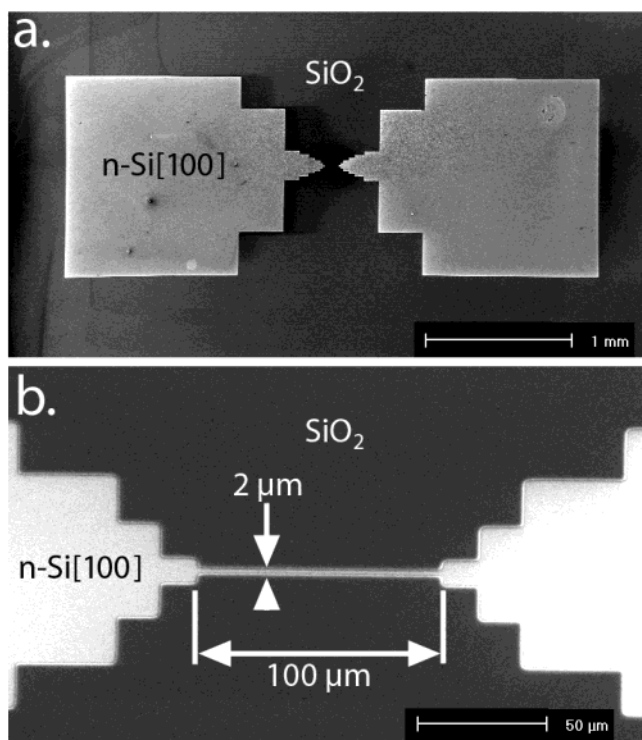


Figure 1. SEM images of the Si patterns produced by optical lithography. (a) Low-magnification overview of one device, (b) higher magnification image of the Si(100) μ -channel. Dark areas in these images correspond to SiO_2 ; bright regions are Si(100).

Sensor Fabrication. After Pd was electrodeposited, H₂ gas sensors were prepared by gluing (conductive liquid silver, Ted Pella, Inc.) a wire or copper tape to both of the 1.4 × 1.4 mm contact pads of a particular device. An optical microscope and a thin glass pipet were used for this purpose.

H₂ Sensing. Sensor measurements were carried out in a sealed ~1.0-mL aluminum cell with two electrical feed-throughs, two gas inlets, and one gas outlet. A MKS Instruments 647C multichannel flow ratio/pressure controller was used in conjunction with MKS 1479A mass flow controllers to control the ratio of H₂ to N₂. N₂ was allowed to flow through the cell continuously, but the H₂ flow was controlled by a Parker-Hannifin Series 9 solenoid valve with a switching time of <5 μs. Sensor resistances were measured with a Keithley 2000 multimeter in a two-wire configuration. The entire gas flow apparatus was controlled with National Instruments LabView 6.0 software.

RESULTS AND DISCUSSION

Electrodeposition of Pd on Patterned *n*-Si(100). A SEM of the pattern employed for sensor fabrication in this paper is shown in Figure 1. This pattern consisted of two large, 1.4 × 1.4 mm squares of exposed Si(100) as seen in Figure 1a. After the deposition of Pd, these two squares facilitated the attachment of electrical contacts to the device. Spanning the 100-μm gap between these contact pads is a 2-μm-wide Si(100) “μ-channel” seen in the SEM image of Figure 1b. Surrounding the exposed Si(100) regions was an electrically insulating oxide layer ~0.1 μm in thickness. In each Pd plating experiment, metal was electrodeposited in parallel onto an electrode surface consisting of four patterns like that shown in Figure 1.

Let us assume that the electrodeposition of hemispherical Pd particles occurs by an instantaneous nucleation and growth mechanism and that these particles are arranged in a hexagonal array. In this case, we can derive an expression for the deposition charge, Q_c , at which these growing Pd particles will coalesce:

$$Q_c = 0.3248nFA/V_m\sqrt{N} \quad (1)$$

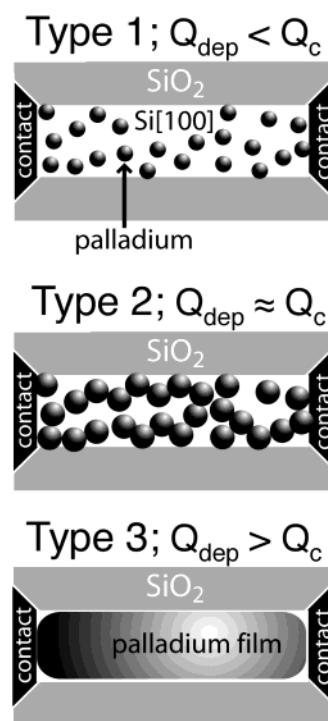
where n is the number of electrons required to discharge one metal ion, F is the Faraday (96485 C equiv⁻¹), N is the nucleation density (cm⁻²), A is the device area on which metal is deposited (cm²), and V_m is the molar volume of metal (8.868 cm³ mol⁻¹ for Pd). For a hexagonal array, the particle radius at coalescence, r_c , is related to N :

$$r_c = (2\sqrt{3}N)^{-1/2} \quad (2)$$

Even though Pd particles actually nucleate randomly on the Si surface (see below), we shall see that the coalescence charge, Q_c , defined by eq 1 provides the basis for delineating three regimes with respect to the quantity of deposited Pd as shown in Scheme 2:

(1) For $Q_{\text{dep}} < Q_c$, the Pd electrodeposit will consist of an ensemble of particles having a mean radius, $r_0 < r_c$. On average, these particles are not in physical contact with one another and “type 1” sensor behavior was observed, as described in detail below.

Scheme 2



(2) For $Q_{\text{dep}} > Q_c$, $r_0 > r_c$ and the coalescence of neighboring Pd particles has occurred producing an electrically continuous network of Pd particles. If a substantial excess of Pd has been deposited beyond Q_c , the holes in this network may become filled producing a solid Pd film. These devices always exhibited “type 3” sensor behavior.

(3) For intermediate quantities of Pd, $Q_{\text{dep}} \approx Q_c$, $r_0 \approx r_c$, and metal particles are just coming into physical contact with nearest neighbors. A percolation threshold for conduction through the Pd electrodeposit along the channel is expected. These devices usually exhibited “type 2” sensor behavior. Next we describe the preparation of Si μ-channel devices using Q_{dep} values that correspond to these three regimes.

The electrodeposition of metals on H₂-passivated Si surfaces usually occurs by a mechanism involving prompt three-dimensional growth of metal islands on the Si surface, irrespective of the crystallographic orientation of the surface.^{4–8} This “Volmer–Weber” mechanism is dominant because of the low surface energy of the coordinately saturated surface. Furthermore, prior work has shown that the Volmer–Weber deposition of metal proceeds by a progressive nucleation and growth mechanism.^{6–9} This means the number of growing metal nuclei increases continuously as a function of deposition time. If the nucleation and growth of Pd occur by a progressive nucleation and growth mechanism, then the three limiting cases shown in Scheme 2 will not be clearly differentiated. For this reason, we employed a deposition scheme intended to enforce instantaneous nucleation and growth of Pd

(4) Ji, C. X.; Oskam, G.; Searson, P. C. *J. Electrochem. Soc.* **2001**, *148*, C746.

(5) Ji, C. X.; Oskam, G.; Searson, P. C. *Surf. Sci.* **2001**, *492*, 115.

(6) Oskam, G.; Searson, P. C. *J. Electrochem. Soc.* **2000**, *147*, 2199.

(7) Oskam, G.; Long, J. G.; Natarajan, A.; Searson, P. C. *J. Phys. E: Appl. Phys.* **1998**, *31*, 1927.

(8) Stiger, R.; Craft, B.; Penner, R. M. *Langmuir* **1999**, *15*, 790.

(9) Allongue, P.; Souteyrand, E. *J. Electroanal. Chem.* **1993**, *362*, 79.

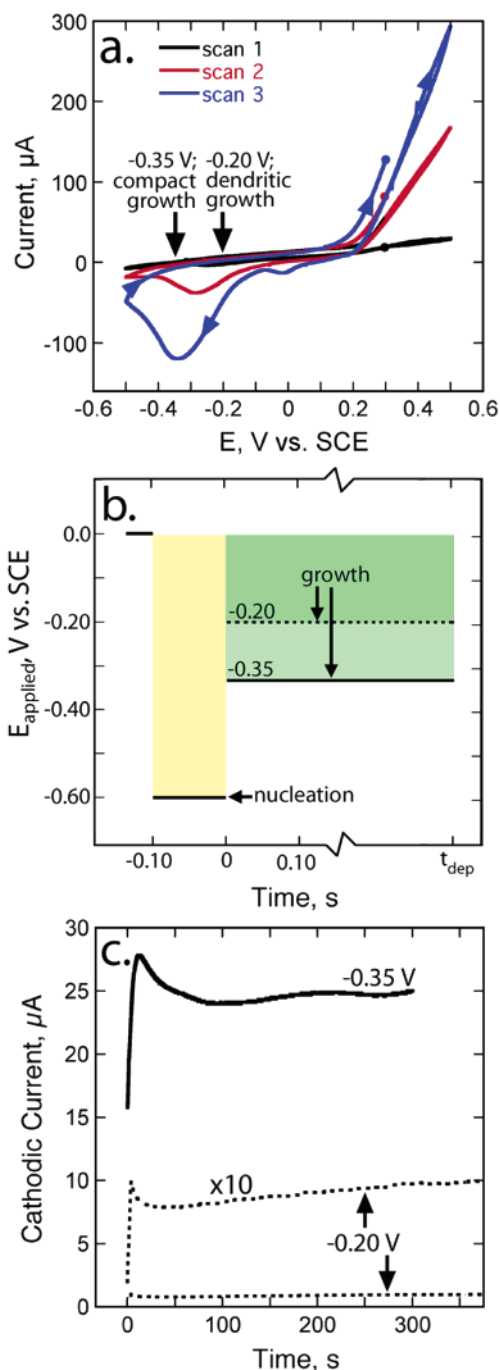


Figure 2. (a) Cyclic voltammogram (20 mV s^{-1}) for four device patterns (in parallel) in the Pd plating solution, (b) schematic diagram of the two-pulse method employed here for the electrodeposition of Pd on Si, and (c) deposition current versus time plotted during the growth phase for Pd electrodeposition carried out at -0.35 and -0.20 V.

within the Si μ -channel. This scheme can be explained with reference to the cyclic voltammogram shown in Figure 2a. The pronounced reduction with an onset at -0.10 V versus SCE corresponds to Pd electrodeposition. An oxidation is also seen in the cyclic voltammograms of Figure 2a, but the processes responsible for this current were not investigated.¹⁰ Instantaneous

(10) Two candidates are oxidative palladium stripping and oxidation of the silicon surface. Since either of these processes would be detrimental to our sensors, silicon surfaces on which palladium was electrodeposited were not anodized.

nucleation and growth of Pd particles was carried out by first pulsing from an initial potential of 0.0 V versus SCE to -0.60 V for 100 ms. This nucleation pulse produced $(4\text{--}6) \times 10^9 \text{ cm}^{-2}$ of Pd nanoparticles on the Si(100) surface. These Pd “seeds” were then grown at either -0.20 or -0.35 V until a specified quantity of Pd had been deposited. At neither of these two growth potentials did the nucleation of new Pd nuclei occur. Thus, this two-pulse waveform (Figure 2b) accomplished two things: First, it restricted the nucleation of Pd to the 100 -ms duration of the -0.60 -V pulse. Second, it provided for growth at a much less negative potential (either -0.2 or -0.35 V) at which nucleation was kinetically unfavorable and at which the growth of Pd metal occurred at a kinetically controlled rate thereby eliminating diffusional coupling^{11,12} between growing Pd particles. Previously,^{13–16} we have shown that these growth conditions favor the formation of metal particles that are very narrowly dispersed in diameter. Two current versus time transients for the electrodeposition of Pd using both -0.20 and -0.35 V growth potentials are shown in Figure 2c. At both potentials, the deposition current was quasi time independent. This deposition current was $200\text{--}300$ -fold higher at -0.35 V than at -0.20 V.

Characterization of the Pd Electrodeposit. Electrodeposited Pd was characterized by resistance measurements, by SEM, and by scanning Auger microprobe (SAM) analysis.

Shown in Figure 3 is a plot of the resistance of a Si(100) channel as a function of the electrodeposition charge for Pd, Q_{dep} . The charge indicated here is the total associated with deposition onto the μ -channel structure and the 2.0-mm^2 contact pads on each end of it (total area 4.0 mm^2). For depositions carried out at a potential of -0.35 V, the resistance of a Si(100) channel decreased dramatically from $\sim 10 \text{ M}\Omega$ to less than $10 \text{ k}\Omega$ as the deposition charge increased to 4 mC . How close is this transition to the calculated value of Q_c ? Based on SEM analysis, the nucleation density produced by the initial $-0.60 \text{ V} \times 100 \text{ ms}$ pulse is in the range from 4×10^9 to $6 \times 10^9 \text{ cm}^{-2}$. Using these values for N and a device area of 0.040 cm^2 , eq 1 yields Q_c values of 3.6 ($N = 6 \times 10^9 \text{ cm}^{-2}$) and 4.6 mC ($N = 4 \times 10^9 \text{ cm}^{-2}$) per device. Therefore, the precipitous resistance drop seen in Figure 3a occurs close to Q_c , and we conclude that it is associated with the coalescence of Pd particles in the μ -channel. As the quantity of Pd was increased further from this point, the resistance of the Si(100) channel decreased more slowly to $\sim 1 \text{ k}\Omega$ at 14 mC . The Pd films obtained at a growth potential of -0.35 V were relatively smooth, as shown in the SEM images of Figure 3b and c. However, this was not the case for films prepared at a growth potential of -0.20 V as shown in Figure 3d and e. Instead, growth at -0.20 V was dendritic in nature, particularly at the edges of the μ -channel. Such films did not exhibit a transition to lower resistance at Q_c , and this is understandable since excess Pd is deposited at the edges of the μ -channel structure; this excess Pd did not contribute to the diameter of Pd particles within the μ -channel. Many devices prepared at -0.20 V with deposition Q_{dep} well above 4 mC were

(11) Franssaer, J.; Penner, R. M. *J. Phys. Chem. B* **1999**, *103*, 7643.

(12) Penner, R. M. *J. Phys. Chem. B* **2001**, *105*, 8672.

(13) Liu, H.; Ng, K.; Zach, M. P.; Penner, R. M. *Electrochim. Acta* **2002**, *47*, 671.

(14) Penner, R. M. *J. Phys. Chem. B* **2002**, *106*, 3339.

(15) Liu, H.; Favier, F.; Ng, K.; Zach, M. P.; Penner, R. M. *Electrochim. Acta* **2001**, *47*, 671.

(16) Liu, H.; Penner, R. M. *J. Phys. Chem. B* **2000**, *104*, 9131.

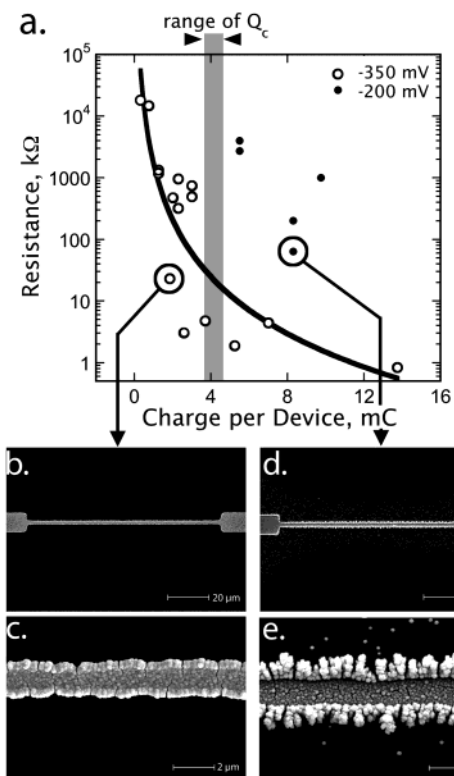


Figure 3. (a) Resistance of Si μ -channels plotted as a function of Q_{dep} , the Pd electrodeposition charge. Shown in gray is the range of Q_c values calculated using eq 1 and a range of nucleation densities, N , from 4×10^9 to 6×10^9 cm^{-2} . (b, c) SEM images of the compact morphologies deposited at -350 mV (these images are of an unusual sensor for which $Q_{\text{dep}} < Q_c$ but which exhibited type 3 sensor behavior); (d, e) SEM images of the dendritic deposits obtained at -200 mV.

found to exhibit type 1 or type 2 device behavior. However, the sensor behavior for devices prepared using dendritic films prepared at -0.20 V was unpredictable, and we focused primarily on sensors prepared using a growth potential of -0.35 V.

Many of the Pd-covered μ -channels prepared during the course of this investigation were analyzed by SEM. The three Pd-covered μ -channels shown in Figure 4 were representative of the morphologies seen for the three sensor types. Each μ -channel was imaged by SEM both before and after exposure to 100% H_2 gas. μ -channels that exhibited type 1 or type 2 sensor behavior had discontinuous Pd electrodeposits (Figure 4, top and middle), and the morphology of these deposits—examined ex situ in the SEM—was not affected on the 0.1 - μm scale by exposure to H_2 .

Continuous Pd electrodeposits, like that shown in Figure 4 (bottom), always cracked upon exposure to 100% H_2 . Mechanical deformations are caused by the stress imposed on the Pd lattice by the 3.5% lattice expansion associated with the $\alpha \rightarrow \beta$ phase transition for Pd hydride.¹⁷ Undoubtedly, these stresses coupled with the embrittlement of the Pd lattice associated with exposure to H_2 ^{18,19} were also responsible for the cracking observed in the Pd films prepared here. As discussed below, these cracks did not

(17) Lewis, F. A. *The Palladium/Hydrogen System*; Academic Press: New York, 1967.

(18) Anderton, C.; Strother, N.; Pote, J.; Foley, R.; Rebeiz, K.; Nesbit, S.; Craft, A. *Scr. Mater.* **1996**, *35*, 1013.

(19) Rebeiz, K.; Craft, A. *J Energy Eng.* **2000**, *126*, 95.

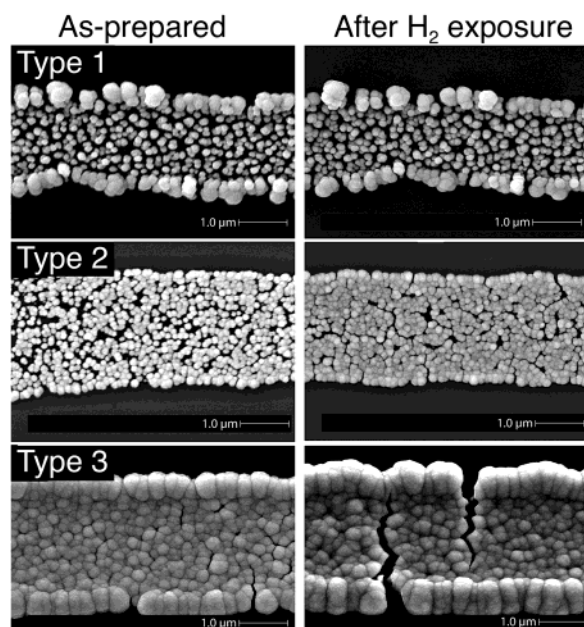


Figure 4. SEM images showing the morphology of typical Pd deposits corresponding to the three sensor types investigated. Deposition potentials and charges were as follows: type 1, $E_{\text{growth}} = -0.20$ V, $Q_{\text{dep}} = 9.75$ mC; type 2, $E_{\text{growth}} = -0.35$ V, $Q_{\text{dep}} = 1.85$ mC; type 3, $E_{\text{growth}} = -0.35$ V, $Q_{\text{dep}} = 13.75$ mC.

contribute to the function of type 3 sensors because they did not completely traverse the μ -channel (thereby forming a break junction).

SAM analysis was also employed to characterize the μ -channel after Pd electrodeposition. In Figure 5a is shown a Si(100) channel onto which size-similar, 200-nm-diameter Pd particles have been deposited. Measurement of the Pd Auger signal as a function of horizontal position at the white line shown in Figure 5a yielded the trace shown in Figure 5b. The positions of the particles seen in Figure 5a correlate with the highest Pd signal intensity seen in this trace. This is the expected result if these particles are composed of elemental Pd. In addition, a Pd signal above background is also observed within the Si(100) channel between Pd particles. Outside of this channel, the Pd Auger signal falls to a value close to zero. These conclusions are supported by the elemental maps of this region acquired by SAM for Pd (Figure 5c) and Si (Figure 5d). One possible explanation for the “residual” Pd Auger signal between Pd particles is the presence of a surface Pd silicide layer. This layer might be formed by the following scenario: Positively charged Pd cations are electrostatically immobilized, but not discharged, at the negatively charged Si(100) surface that exists during electrodeposition. If this adsorbed Pd survived emersion, it would be susceptible to reduction to Pd^0 and this would immediately result in the formation of a surface Pd silicide layer.²⁰ A second possible explanation for the Pd signal seen between particles is that the spatial resolution of the Auger probe is affected by scattering of the primary electrons and secondary electrons causing Auger emission from the Pd particles, which is then detected. Both of these explanations are highly speculative, and additional surface analysis investigations will be required to determine whether a surface Pd silicide is

(20) Anton, R.; Neukirch, U.; Harsdorff, M. *Phys. Rev. B* **1987**, *36*, 7422.

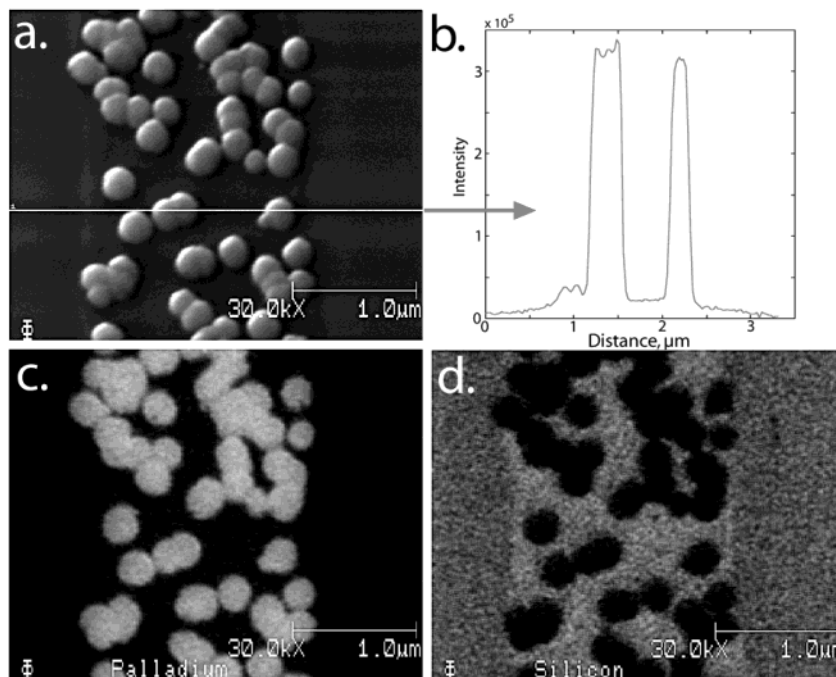


Figure 5. Scanning Auger microprobe analysis of the Pd clusters in the active area of the device. (a) SEM image of the analyzed area, (b) Pd Auger signal versus position corresponding to the location of the horizontal white line in (a); (c) Pd Auger map, and (d) Si Auger map (Pd and Si, respectively, appear white in these maps).

indeed present and to determine whether this layer played any role in the detection of H_2 gas by these devices.

Characterization of Pd/Si μ -Channel H_2 Detectors. The properties of Pd-covered Si μ -channels for detecting H_2 gas changed dramatically with the quantity of deposited Pd metal. Three distinct device behaviors were observed and sensors of “type” 1, 2, or 3 were defined according to the relative resistance change of the μ -channel, $\Delta R/R_0$, as the contacting gas phase was cycled between pure nitrogen and 20% H_2 in N_2 : type 1, $\Delta R/R_0$ decreased in H_2 to -25% or less; type 2, $\Delta R/R_0$ decreased for H_2 concentrations below 2% and then increased asymptotically to $\sim -8\%$ at high H_2 concentrations; type 3, $\Delta R/R_0$ increased in H_2 and was $+5\%$ or less. As we have already indicated, these device behaviors correlated with a Pd deposition charge that was lower than Q_c (type 1), higher than Q_c (type 3), or approximately equal to Q_c (type 2). Based on the data of Figure 3a, we expect that the sensor resistance measured in air should decrease in the order type 1, type 2, type 3, and as shown in Figure 6, this expectation is fulfilled.

Figure 7 shows the response of these sensors to 1-s pulses of H_2 at three concentrations. A typical type 1 sensor exhibited a negative $\Delta R/R_0$ that increased in amplitude to -20% with increasing H_2 concentration, as shown in Figure 8. Although, as shown in Figure 7, type 1 sensors responded rapidly to increases in H_2 , these sensors were much slower (>60 s) to respond to decreases in the H_2 concentration and were similar in this regard to type 3 sensors. A series of control experiments proved to us that the observed response for type 1 sensors was unrelated to the detailed properties of the Pd/Si μ -channel. In fact, lithographically defined contact pads, separated from one another by 100 – 200 μm and covered with Pd metal, exhibited a type 1 sensor response even when no Pd/Si μ -channel was present between them. No response to H_2 was observed for μ -channels onto which no palladium metal

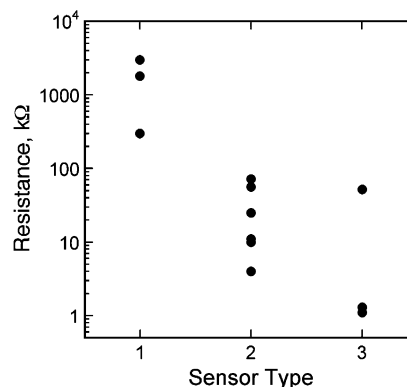


Figure 6. Resistance of the sensors vs. sensor type. In general, the resistance of Pd–Si μ -channel sensors was greatest for sensors exhibiting a type 1 response and lowest for sensors exhibiting a type 3 response to H_2 .

was deposited. We discuss the probable origin of this response in the next section.

The response of type 2 H_2 sensors (Figure 7) was similar to type 1 sensors except that both the response time and the recovery time were somewhat faster. The type 2 sensor examined in Figure 7, for example, showed a $\Delta R/R_0$ in 1% H_2 of between -15 and -20% . However, as shown in Figure 8, the calibration curve for type 2 sensors was qualitatively different from that for either type 1 or type 3 sensors: As the H_2 concentration was increased from 0.25%, $\Delta R/R_0$ first increased slightly (to $+0.7\%$) before decreasing rapidly to $\sim -20\%$ as the H_2 concentration increased to near 1% H_2 . Above 1% H_2 , $\Delta R/R_0$ again increased asymptotically to between -5 and -7% . The LOD for type 2 sensors was reproducibly in the range from 0.5 to 1%. Whereas the “turn-on” rate for type 2 sensors in H_2 was comparable to type 1 and type 3 sensors, in the absence of H_2 , type 2 sensors returned to the baseline

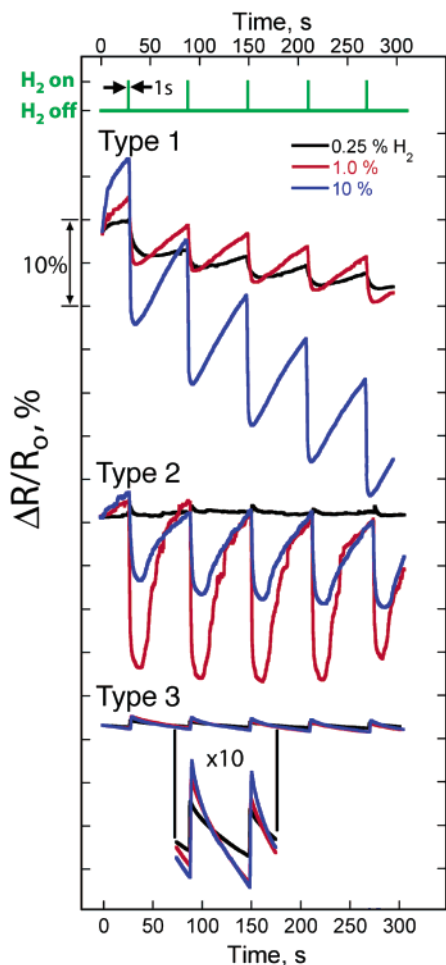


Figure 7. Percent change of the resistance, $\Delta R/R_0$, vs time for the three different types of sensors at three different H_2 concentrations, as indicated. The Pd electrodeposition conditions and R_0 for each sensor were as follows: type 1, $E_{\text{growth}} = -0.20$ V, $Q_{\text{dep}} = 5.50$ mC, $R_0 = 6.2$ M Ω ; type 2, $E_{\text{growth}} = -0.35$ V, $Q_{\text{dep}} = 1.85$ mC, $R_0 = 9.4$ k Ω ; type 3, $E_{\text{growth}} = -0.35$ V, $Q_{\text{dep}} = 5.25$ mC, $R_0 = 1.2$ k Ω . The H_2 pulse had a duration of 1 s, and the time between pulses (in pure nitrogen) was 60 s.

resistance in less than 60 s. The complex response seen in Figure 8 for type 2 sensors disqualifies them for use as general purpose H_2 sensors, but these devices nevertheless produced a signal (a reduced resistance) for 0.5% hydrogen that can be distinguished from noise with a high degree of certainty ($>2\sigma$). Moreover, after $\Delta R/R_0$ increases in amplitude to -20% (at 1% H_2), the amplitude of $\Delta R/R_0$ never drops below -5% even for 100% H_2 . In other words, a $\Delta R/R_0$ of -5% or less, achieved for a minimum H_2 concentration below 1%, is a reliable signal that H_2 concentrations are in a dangerous range. This is a limited but still highly significant claim because this means a type 2 sensor is capable of functioning as a H_2 safety sensor.

Type 2 sensors were obtained for devices on which the Pd deposition charge was in the range from 1.5 to 5 mC provided the deposition was carried out at $E_{\text{growth}} = -0.35$ V. Depositions carried out at $E_{\text{growth}} = -0.20$ V often produced type 2 sensors at much higher deposition charges, for reasons already discussed above.

Remarkably, the *direction* of the resistance change seen for type 3 sensors was opposite to that seen for either type 1 or type

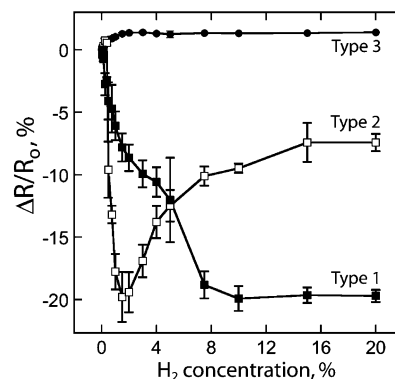


Figure 8. Typical calibration plots ($\Delta R/R_0$ vs H_2 concentration) for the three different sensor types for H_2 concentrations in the range from 0.05 to 20%. \square , Type 1: $E_{\text{growth}} = -0.20$ V; $Q_{\text{dep}} = 5.50$ mC. \blacksquare , Type 2: $E_{\text{growth}} = -0.35$ V; $Q_{\text{dep}} = 1.85$ mC. \bullet , Type 3: $E_{\text{growth}} = -0.35$ V; $Q_{\text{dep}} = 5.25$ mC. In all cases, the H_2 pulse had a duration of 1 s, and the time between pulses (in pure nitrogen) was 60 s.

2 devices, and the amplitude of $\Delta R/R_0$ was much smaller. Specifically, the type 3 sensor examined in Figure 7 showed $\Delta R/R_0 = +1.5\%$ in 10% H_2 , and $+0.75\%$ in 0.25% H_2 . The LOD for this sensor was close to 0.10% H_2 —a technologically useful lower limit—but as shown in the calibration curve of Figure 8, its $+1.5\%$ maximum $\Delta R/R_0$ was constant for H_2 concentrations ranging from 3 to 20%. This $\Delta R/R_0$ is much smaller than predicted for a simple palladium resistor, which will exhibit a monotonically increasing resistance with increasing H_2 concentration, and a $\Delta R/R_0$ of $+100\%$ when it is equilibrated with pure H_2 gas.¹⁷ The origin of this response is discussed in the next section. The temporal properties of the response shown in Figure 7 were typical of that seen for many type 3 devices: These sensors responded rapidly (<1 s) to increases in the H_2 concentration but were very slow (>50 s) to respond to decreases in the H_2 concentration. In general, type 3 sensors were obtained for devices on which the Pd deposition charge exceeded 4 mC provided the deposition was carried out at $E_{\text{growth}} = -0.35$ V.

Mechanisms of Operation for Pd/Si μ -Channel H_2 Detectors. The responses seen for all three types of H_2 sensors can be understood on a qualitative basis in terms of the three mechanisms depicted schematically in Figure 9.

For devices based on the lithographic pattern shown in Figure 1, two possible paths for current flow exist: through the Si and through the Pd electrodeposit. If no continuous path for current through the Pd electrodeposit exists—as in a type 1 sensor—then current will flow from the incomplete Pd layer at one contact pad into the Si and back out again the same way at the other contact pad. In this case, the only possible mode for H_2 sensing involves the properties of the Pd–Si interfaces that are present at each contact pad. It is well established that Pd/*n*-Si Schottky diodes are responsive to H_2 .^{1,2,21–23} The origin of the response derives from a decrease in the work function of the Pd layer, ϕ_{PdH_x} , as the hydrogen stoichiometry in the presence of H_2 gas increases from $x = 0$ to $x = 0.7$. The detailed mechanism of work function

(21) Shivaraman, M. S.; Lundstrom, I.; Svensson, C.; Hammarsten, H. *Electron. Lett.* **1976**, *12*, 484.

(22) Kang, W. P.; Gurbuz, Y.; Davidson, J. L.; Kerns, D. V. *J. Electrochem. Soc.* **1994**, *141*, 2231.

(23) Kang, W. P.; Gurbuz, Y. *J. Appl. Phys.* **1994**, *75*, 8175.

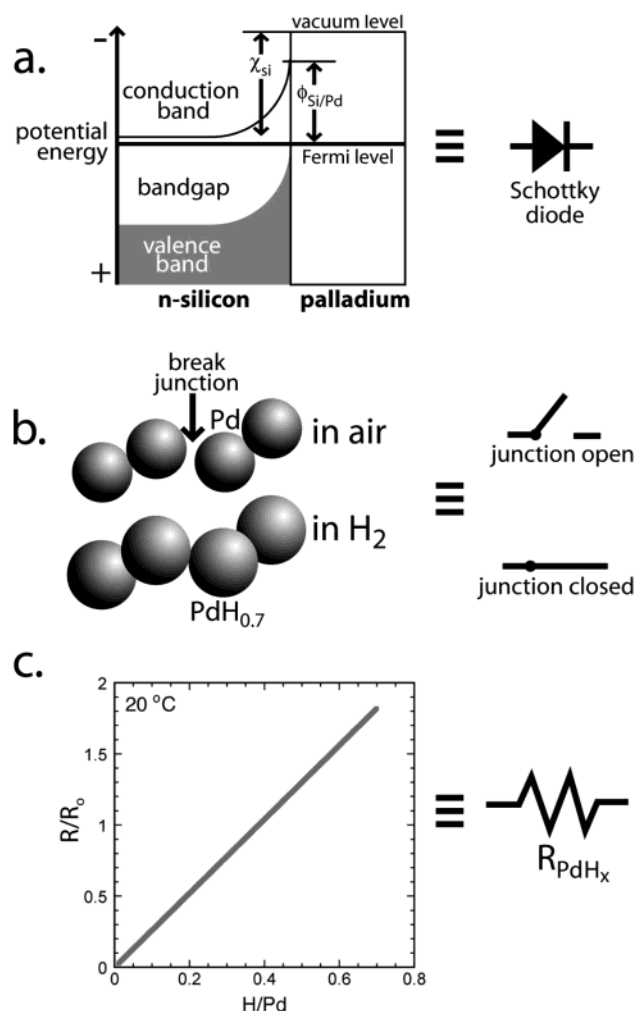


Figure 9. Three mechanisms that contribute to the conductivity of the Pd–Si μ -channel structures investigated in this study. Shown at right are the symbols for each mechanism used in Figure 11. (a) Schottky diode formation between Pd metal and Si. ϕ_{PdH_x} is the work function of the Pd ($x = 0$) or Pd hydride ($x > 0$) layer, ϕ_{barrier} is the barrier height of the Schottky diode, and χ_{Si} is the electron affinity of Si ($\chi_{\text{Si}} = 4.05$ eV).²⁸ (b) A H_2 -responsive break junction, or switch, that cycles between an open and closed state as Pd hydride cycles between the α - and β -phases. The β -phase of Pd hydride has a lattice constant that is 3.5% greater than the α -phase. (c) Increased resistance of PdH_x as a function of x after ref 17.

lowering in this system is complex and beyond the scope of this study.²⁴ The band diagram of Figure 9a shows that as the work function of the Pd contact is reduced, the barriers—both forward and reverse—to charge transport across this interface are reduced. Increased current flow is therefore seen both in forward bias (direction of electron flow from Si to Pd) and in reverse bias for these interfaces in the presence of H_2 .^{2,21,23,25} Does this effect manifest itself for the Pd/*n*-Si interfaces produced at the contact pads in these experiments? The data shown in Figure 10 demonstrate that these contact pads can function as H_2 -responsive Schottky barriers. In this experiment, a continuous Pd film was electrodeposited onto a Si(100) surface and the current versus voltage properties of this interface were probed using an ohmic

(24) Lundstrom, I. *Sens. Actuators* **1981**, 403.

(25) Kim, C. K.; Lee, J. H.; Lee, Y. H.; Cho, N. I.; Kim, D. J.; Kang, W. P. *J. Electron. Mater.* **1999**, 28, 202.

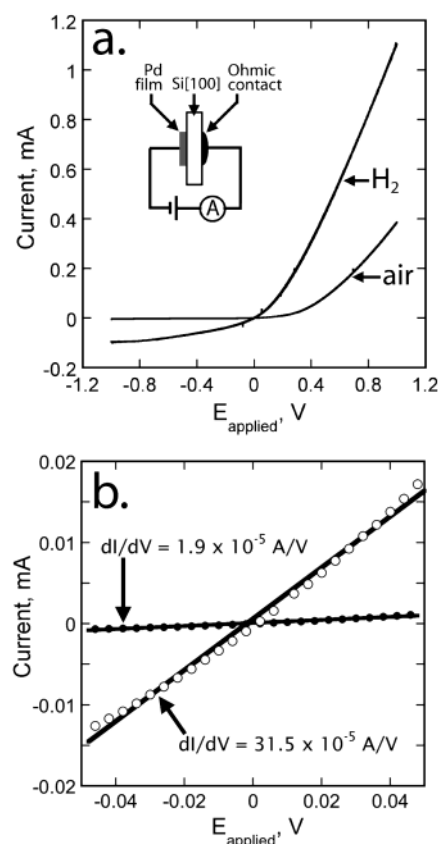


Figure 10. (a) Current vs E_{applied} (Pd versus Si) for a Pd Schottky diode prepared by the electrodeposition of a Pd film (~ 100 mC cm^{-2}) onto a clean H -terminated Si(100) electrode. Shown are I – V curves obtained in air and in 100% H_2 . (b) Expanded view of the low-bias (± 50 mV) region of the same curves shown in (a). The low-bias behavior of the Pd–Si interface is close to ohmic; the resistance is much higher in air than in H_2 .

back contact. In the absence of H_2 , conventional Schottky diode behavior is observed; in the presence of H_2 , higher current in both forward and reverse directions is seen, signaling the lowering of the Pd work function by hydride formation. The Keithley 2000 multimeter employed for resistance measurements in this study tracks the sensor resistance near the low bias limit. As shown in Figure 10b, at small biases ($|E_{\text{applied}}| < 50$ mV), both I – V curves are pseudoohmic and therefore the measured resistance is independent of the direction of current flow. For the interface probed in Figure 10, this resistance was 15 times higher in air than in H_2 . Based on this analysis, the sensor equivalent circuit for a type 1 sensor consists simply of a series combination of two H_2 -responsive Schottky diodes—one at each contact pad is as shown in Figure 11.

Type 3 sensors exhibit an increased resistance in H_2 , not a decreased resistance as seen for both type 1 and type 2 sensors (see below). The magnitude of this resistance change was also much smaller ($\Delta R/R_0 < +5\%$) than seen for the other two sensor types. Two mechanisms seem to operate in parallel to produce these two properties. The dominant mechanism is the linear increase in the electrical resistance of Pd hydride, PdH_x , with the hydrogen stoichiometry, x (see Figure 9c).¹⁷ This mechanism forms the basis for the operation of all Pd resistor-based H_2 sensors. However if this were the only mechanism operating, $\Delta R/R_0$ would be expected¹⁷ to approach +100% upon exposure to pure

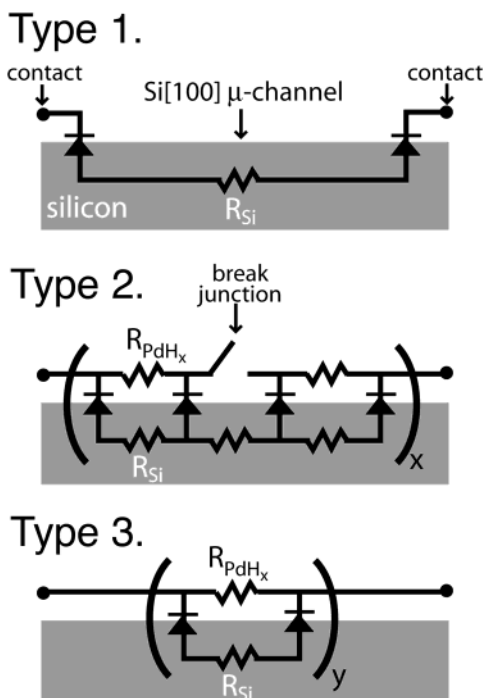


Figure 11. Sensor equivalent circuits representing the mechanisms operating in Pd/Si μ -channel H_2 sensors. The mechanisms associated with each symbol are detailed in Figure 9.

H_2 at room temperature, and this is not observed. A second mechanism that decreases the resistance of the μ -channel must act in opposition to this effect. The logical candidate is the same Schottky barrier mechanism that is responsible for the type 1 sensor response. The interplay of these two mechanisms occurs via the sensor equivalent circuit shown in Figure 11. When the Pd electrodeposit becomes electrically continuous along the 100- μ m length of the μ -channel, a voltage divider is created that partitions current between the Pd layer, R_{PdH_x} , and the Si substrate, R_{Si} . In the presence of H_2 , the branching ratio is altered by two H_2 -sensitive circuit elements: R_{PdH_x} (increases in the presence of H_2), and the Pd/Si Schottky barrier (resistance decreases in the presence of H_2). These two circuit elements operate in parallel to divert current into the Si substrate during H_2 exposure with the result that the measured resistance change for the μ -channel is reduced from the expected +100% in pure H_2 at 25 °C. We postulate that the equivalent circuit for a type 3 sensor shown in Figure 11 provides the basis for the small $\Delta R/R_0$ values seen in the data of Figures 7 and 8, for example.

Finally we consider the mechanism for type 2 sensors. Relative to type 1 and type 3 sensors, type 2 sensors possessed two unique properties: First, type 2 sensors exhibited a faster recovery time of <60 s. In contrast, recovery from a 1-s H_2 exposure for type 1 or type 3 sensors requires 60–120 s (see Figure 7a, c). Second, as already discussed, type 2 sensors exhibited a complex, peaked calibration curve. We believe the sensor equivalent circuit shown in Figure 11 is responsible for both of these attributes. This circuit is similar to that for a type 3 sensor except for the addition of break junctions—or switches—in the Pd layer. As shown schematically in Figure 9b, these break junctions exist because the lattice constant of the FCC β -phase of Pd hydride is 3.5% larger than that of the α -phase.¹⁷ This volume change causes nanometer-scale gaps between Pd particles in the μ -channel to reversibly close

and open in response to the presence and absence of H_2 , respectively. We postulate that this mechanical component of the sensor response mechanism imparts the recovery time that is characteristic of type 2 sensors.

The existence of break junctions in the Pd film is also the likely origin of the peaked calibration curve seen for type 2 sensors. Based on the known properties of the $\alpha \rightarrow \beta$ phase transition,¹⁷ these break junctions are expected to close at a threshold H_2 partial pressure of 7–8 Torr ($\approx 1\%$ H_2 at sea level). This threshold matches the H_2 concentration at which the largest response is observed for type 2 sensors. For H_2 concentrations above 1%, the film is purely β -phase, all break junctions within the Pd film that are capable of closing have closed, and the film structure is invariant. The increased resistance of the β -phase PdH_x in the concentration regime above 1% (see Figure 9c) is responsible for the asymptotic increase in the resistance of type 2 sensors in this concentration regime.

The mechanism for a type 2 Pd–Si μ -channel is related to the mechanism for H_2 sensors that are based on arrays of Pd nanowires,^{26,27} and the performance of these devices is also similar in terms of the direction of the resistance change (lower R_{sensor} in H_2), the rapid temporal response (<1-s turn-on), and the concentration range over which H_2 is detected. In the latter regard, the type 2 Pd–Si μ -channel was superior because a LOD of less than 0.50% was routinely observable (Figure 8) whereas Pd nanowire arrays show a LOD of $\sim 2\%$.^{26,27} We attribute the lower LOD of type 2 sensors to the Schottky barriers that are distributed along the Si μ -channel. It is well-established^{1,2,21} that Pd Schottky diodes on Si are capable of detecting H_2 in the 10–100 ppm range. Type 1 sensors, which rely entirely for their response on Schottky barriers, exhibited a similar LOD (Figure 8). It is likely that the concentration dependence seen for type 2 sensors derives, in part, from an increase in the number of low-impedance paths through the Pd film as the number of closed break junctions increases with increasing H_2 concentration. Again, this behavior is analogous to that of Pd nanowire arrays.^{26,27} From a technological perspective, the similarity between the type 2 sensors produced here and the Pd nanowire array sensors described earlier is significant because fabrication of the Si μ -channel based sensors involves standard Si microfabrication technology.

SUMMARY

The preparation and characterization of Pd-covered 2 μ m \times 100 μ m Si(100) μ -channels are reported. These μ -channels exhibit large, reversible resistance changes upon exposure to H_2 gas. The most important conclusions of this investigation are the following:

(1) Pd can be electrodeposited onto Si(100) surfaces under instantaneous nucleation and growth conditions that permit a well-defined coalescence charge, Q_c , to be defined (eq 1).

(2) The quantity of deposited Pd, Q_{dep} , relative to Q_c provides control over the resistance change observed for Si μ -channels in H_2 sensors. The variation in the observed sensor response is dramatic: with increasing Q_{dep} , an inversion of the response of a Pd-covered Si μ -channel was observed in this study.

(26) Favier, F.; Walter, E. C.; Zach, M. P.; Benter, T.; Penner, R. M. *Science* **2001**, 293, 2227.

(27) Walter, E. C.; Favier, F.; Penner, R. M. *Anal. Chem.* **2002**, 74, 1546.

(28) Sze, S. M. *Physics of Semiconductor Devices*; John Wiley & Sons: New York, 1981.

(3) Three discrete types of sensor responses to H₂ were observed as the Pd coverage is increased. In terms of response time, sensitivity, and power efficiency, the type 2 sensors demonstrated here come close to meeting all of the requirements for mobile H₂ gas safety sensing applications; *however, type 2 devices would not be good general use H₂ sensors because of the peaked calibration curve that was observed.* A type 2 sensor exhibited a LOD below 1%, a response time of less than 1 s, and a recovery time of less than 60 s. Because these devices operate at ambient temperature, they can be configured to draw less than 1 μW of power.

(4) Three mechanisms contribute to the behavior of Pd μ-channel H₂ sensors. We believe that these sensors are the first to exploit multiple mechanisms for detecting H₂ in a single device. For type 2 and type 3 sensors, more than one of these mechanisms operate simultaneously to produce the observed sensor characteristics.

Although the principle of multimode H₂ detection has been demonstrated here, we have not addressed several key issues in

this initial study. These include the stability of the response to H₂ for Pd-covered Si μ-channels as a function of time for extended periods (weeks and months), the effect of humidity and temperature on device response properties, and the “process latitude” of sensor fabrication especially in terms of the quantity of Pd that is electrodeposited. We have also not attempted to optimize our sensors to improve performance. Key parameters to be investigated in future studies include the Si dopant density, the μ-channel dimensions, and the composition of the electrodeposited metal.

ACKNOWLEDGMENT

This work was funded by the NSF (Grant CHE-0111557) and by the UC Discovery Program in conjunction with Nanomix Inc. (Grant biostar01-10169). The authors also gratefully acknowledge the financial support of G.K. by DaimlerChrysler AG.

Received for review May 13, 2003. Accepted July 3, 2003.

AC034507E